







Element-sensitive x-ray absorption spectroscopy and magnetometry of $\text{Lu}(\text{Fe}_{0.2}\text{Mn}_{0.2}\text{Co}_{0.2}\text{Cr}_{0.2}\text{Ni}_{0.2})\text{O}_3$ high-entropy oxide perovskite thin films

Alan Farhan ^{1,2,*}, Maria Cocconcelli ^{1,3}, Federico Stramaglia ⁴, Nikolai Kuznetsov,¹ Lukáš Flajšman ¹, Marcus Wyss ⁵, Lide Yao,⁶ Cinthia Piamonteze,⁴ and Sebastiaan van Dijken ¹

¹*Department of Applied Physics, Aalto University School of Science, P.O. Box 15100, FI-00076 Aalto, Finland*

²*Department of Physics, Baylor University, Waco, Texas 76798, USA*

³*Dipartimento di Fisica, Politecnico di Milano, I-20133 Milano, Italy*

⁴*Paul Scherrer Institute, Forschungsstrasse 111, CH-5232 Villigen PSI, Switzerland*

⁵*Swiss Nanoscience Institute, University of Basel, CH-4056 Basel, Switzerland*

⁶*OtaNano-Nanomicroscopy Center, Aalto University School of Science, P.O. Box 15100, FI-00076 Aalto, Finland*



(Received 7 September 2022; accepted 28 March 2023; published 7 April 2023)

We present a study on the structural and magnetic properties of $\text{Lu}(\text{Fe}_{0.2}\text{Mn}_{0.2}\text{Co}_{0.2}\text{Cr}_{0.2}\text{Ni}_{0.2})\text{O}_3$ (Lu5BO) high-entropy oxide perovskite thin films. We use synchrotron-based x-ray absorption spectroscopy employing x-ray magnetic circular and linear dichroism (XMCD and XMLD) to perform an element-sensitive study on single-crystal epitaxial Lu5BO thin films. Together with XMCD magnetometry, the results reveal dominant antiferromagnetic order with a transition temperature around 100 K.

DOI: [10.1103/PhysRevMaterials.7.044402](https://doi.org/10.1103/PhysRevMaterials.7.044402)

I. INTRODUCTION

The recent introduction of high-entropy oxides (HEOs) has attracted a significant amount of research activities [1–3], as a source for new promising dielectrics [4], multifunctional semiconductors [5], and materials of low thermal conductivity [6]. The key ingredient in high-entropy stabilization is the combination of a large number of cations in equiatomic proportions, resulting in single-phase crystallization. This concept has recently been expanded to high-entropy oxide perovskites (HEOPs), both in the bulk [7,8] and thin film [9–12]. HEOP thin films are particularly attractive, as thin film growth, for example via pulsed laser deposition (PLD), offers single-crystal stabilization mechanisms that go beyond the entropy-driven process. This includes substrate-driven stabilization, laser fluence, oxygen pressure, and growth temperature. Growth-induced stabilization enables HEOP thin films that would potentially not exist in the bulk. Taking the general perovskite formula ABO_3 (A : rare-earth ion and B : $3d$ transition metal ion) into account, it provides a seemingly unlimited freedom to tune the structural and magnetic responses by varying stoichiometries within the transition metal B -site or rare-earth A -site ions, as demonstrated for La-based HEOP thin films [11,12]. Our recent x-ray absorption study on $\text{Tb}(\text{Fe}_{0.2}\text{Mn}_{0.2}\text{Co}_{0.2}\text{Cr}_{0.2}\text{Ni}_{0.2})\text{O}_3$ (Tb5BO) thin films revealed the emergence of long-range ferromagnetic order, mostly driven by X - O - Y superexchange interactions involving primarily Mn^{4+} such as Mn^{4+} - O - Co^{2+} and Mn^{4+} - O - Ni^{2+} , which is supported by the presence of high-spin Co^{2+} populating up to 23% of the Co sites and a 100% proportion of Ni^{2+} [13]. This raises the question how the

overall electronic configuration of transition metal ions changes, when replacing Tb on the rare-earth A sites with another rare-earth element.

Here, we aim to shed light into this question by placing Lu on the A sites, thus growing $\text{Lu}(\text{Fe}_{0.2}\text{Mn}_{0.2}\text{Co}_{0.2}\text{Cr}_{0.2}\text{Ni}_{0.2})\text{O}_3$ (Lu5BO) thin films on (001)-oriented SrTiO_3 (STO) substrates, providing a direct comparison to the previously grown Tb5BO thin films on STO (001) [13]. Lu, being the rare-earth ion with the smallest ionic radius within the lanthanide series, provides an interesting case, regarding HEOP thin films, for multiple reasons. First, Lu-based perovskite thin films such as LuFeO_3 or LuMnO_3 exhibit multiferroic properties [14–16]. Second, due to the small atomic radius of Lu, it is known that the stabilization of other Lu-based perovskites, for example LuNiO_3 , requires growth under high-pressure conditions [17], thus posing the question whether single-crystal Lu5BO thin films can be grown at all, using simple growth conditions similar to those employed in recent studies on other HEOP thin films [9,10,13].

The paper is organized as follows: We begin with a Methods section, where all experimental aspects are discussed, starting from thin film growth to structural and magnetic characterization. This is followed by a section where all experimental results are presented and discussed, before the paper is concluded with a summarizing section.

II. EXPERIMENTAL METHODS

Lu5BO thin films were grown on TiO_2 -terminated STO (001) substrates using a KrF excimer laser ($\lambda = 248$ nm) at a fluence of 1.42 J/cm² and a repetition rate of 5 Hz under an oxygen partial pressure of 0.14 mbar. The substrate temperature was set at 840 °C. The target-to-sample distance was 5.5 cm. We used 14 000 laser pulses to grow thin films

*alan_farhan@baylor.edu

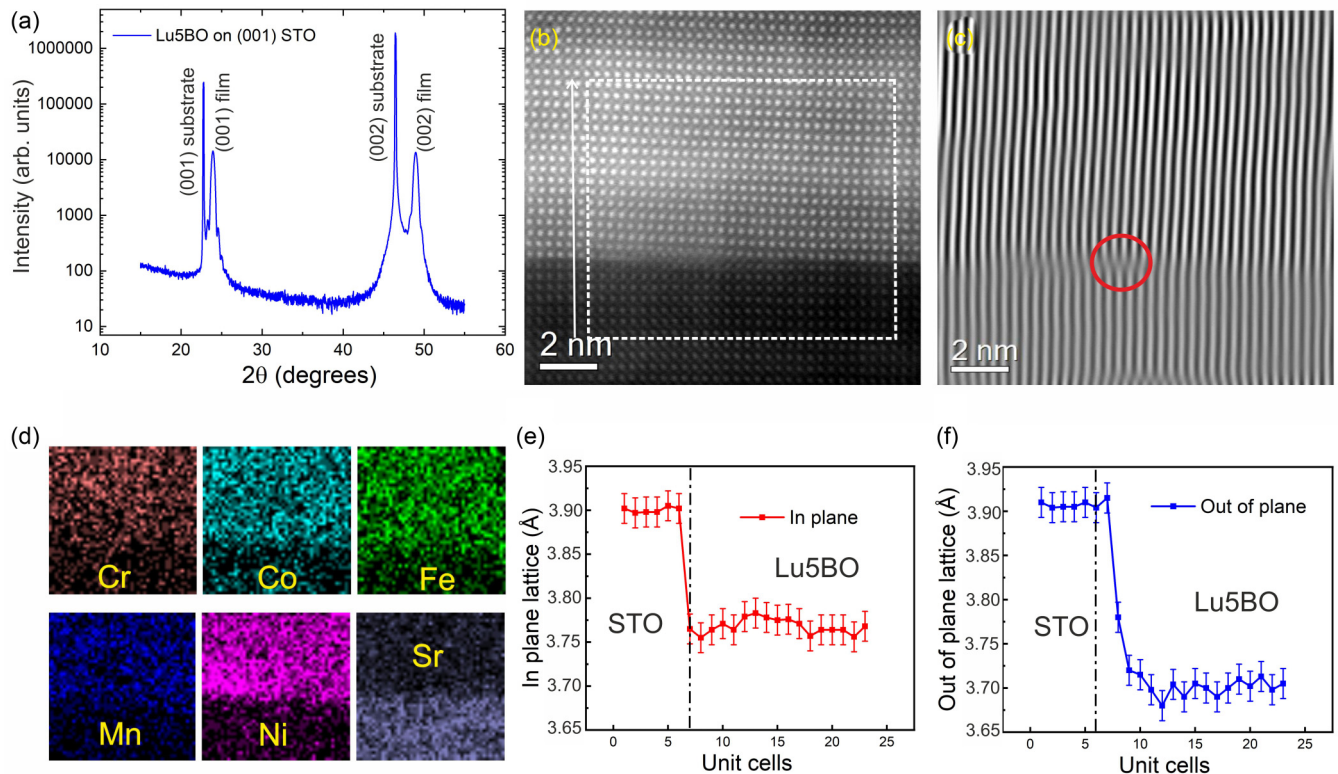


FIG. 1. (a) XRD scan of a 12-nm-thick Lu5BO film grown on a (001)-oriented STO substrate. The XRD scan indicates good single-crystal growth without the presence of secondary phases. (b) Scanning transmission electron microscopy (STEM) image of the same sample along the [100] direction revealing proper epitaxy with some defect structures near the interface. (c) Fast Fourier transform (FFT) of the same section shown in (b), highlighting dislocations emerging at the substrate/film interface. (d) Electron dispersive x-ray spectroscopy (EDX) revealing an isotropic and random distribution of the transition metal elements within the same field of view as shown in (b). (e) and (f) In-plane lattice parameter a and out-of-plane lattice parameter c extracted for a region along the white box highlighted in (b).

with a thickness of 12 nm. Following growth, the films were cooled down under an oxygen pressure of 100 mbar with a cooling rate of 4°C/min. X-ray diffraction (XRD) patterns were recorded using a Rigaku Smartlab high-resolution four-circle x-ray diffractometer. Microstructural characterization and elemental mapping were performed using a JEOL 2200FS scanning transmission electron microscope (STEM) with an electron dispersive x-ray (EDX) spectrometer. Magnetic hysteresis loops were recorded, using a superconducting quantum interference device (SQUID) magnetometer from Quantum Design. Element-sensitive x-ray absorption spectroscopy was performed at the XTreme beamline of the Swiss Light Source [18], employing x-ray magnetic circular and linear dichroism (XMCD and XMLD) at the $L_{2,3}$ edges [19,20] of all five transition metal B -block elements within Lu5BO.

III. RESULTS and DISCUSSION

A. Structural, compositional, and magnetic characterization

The XRD pattern shown in Fig. 1(a) reveals that the Lu5BO thin film on STO (001) is single crystalline with an out-of-plane lattice parameter $c = 3.717 \text{ \AA}$. A comparison to the lattice parameter of the underlying cubic STO (001) substrate ($a = b = c = 3.905 \text{ \AA}$) indicates a lattices mismatch of around 5% and the likely growth of a relaxed film. This

agrees with the STEM image displayed in Fig. 1(b) and the extracted in-plane and out-of-plane lattice parameters near the STO/Lu5BO interface [Figs. 1(e) and 1(f)]. The STEM measurement indicates that the large lattice mismatch between the STO substrate and Lu5BO film relaxes rapidly through defect formation within the first three unit cells of the film, also seen from a fast Fourier transformation (FFT) analysis [see the highlighted region in Fig. 1(c)]. After this, Lu5BO grows as a single-crystal relaxed film onto STO (001) with an average c/a ratio of 0.989 ± 0.003 . Elemental mapping with EDX within the imaged area of the film reveals a homogeneous distribution of the transition metal elements (Fe, Ni, Co, Mn, and Cr), without signs of clustering of individual elements [see Fig. 1(d)].

Following structural characterization, the thin films were forwarded for macroscopic magnetic characterization with SQUID magnetometry. In Fig. 2 we show magnetic hysteresis loops of a 12-nm-thick Lu5BO film recorded at 2.5 K with the magnetic fields applied in plane [see Fig. 2(a)] and out of plane [see Fig. 2(b)], with respect to the surface of the substrate. While the in-plane hysteresis remains practically closed, we observe a wasp-shaped hysteresis loop for the out-of-plane field configuration. The shape of the out-of-plane hysteresis loop resembles that of previously studied high-entropy oxide perovskite thin films such as La5BO [9] and Tb5BO [13]. However, the magnetic moment per unit cell is

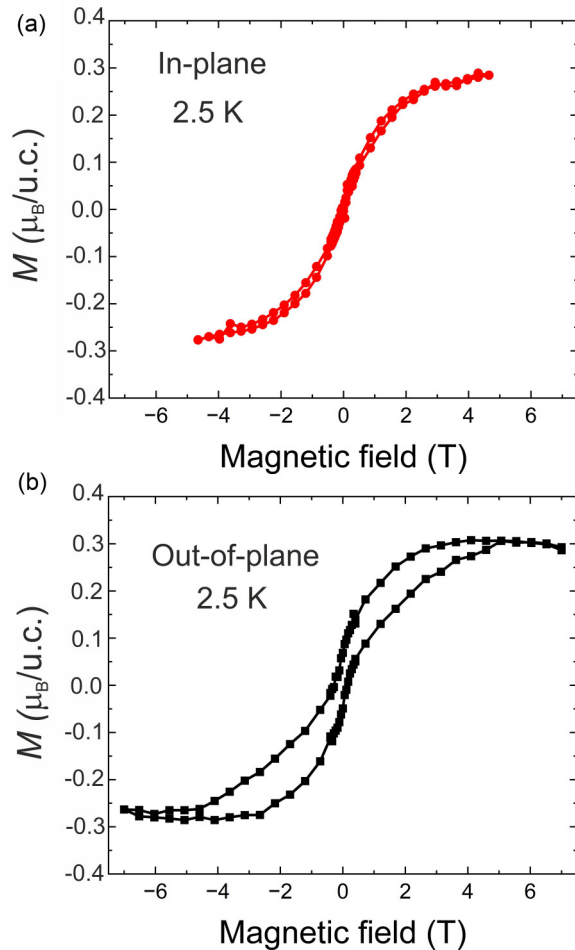


FIG. 2. SQUID magnetic hysteresis loops measured at 2.5 K on a 12-nm-thick Lu5BO film, with magnetic fields applied (a) in plane and (b) out of plane, with respect to the substrate surface.

more than two times smaller in Lu5BO compared to Tb5BO thin films grown on the same substrate [13].

Next, we discuss XMCD spectroscopy measurements on Lu5BO around the $L_{2,3}$ absorption edges of all involved five transition metal elements (Fe, Ni, Co, Mn, and Cr) using both circular right ($c+$) and circular left ($c-$) polarized

x rays (Fig. 3 upper panels). The XAS measurements were performed by total electron yield (TEY) detection [18] at 2.5 K in an out-of-plane geometry, where both the magnetic field (6 T) and x rays are perpendicular to the surface. In addition to this out-of-plane geometry, we performed the same measurements where the magnetic field (6 T) and x rays are employed at a grazing angle of 30° (see Supplemental Material [21]). Subtracting $c+$ and $c-$ spectra from one another gives the normalized XMCD signal for all five transition elements (Fig. 3 lower panels). Added to Fig. 3 are comparisons of the experimental XAS and XMCD spectra (black lines) and simulations performed with CTM4XAS [22] using multiplet ligand field theory (red, green, and blue lines). The computations are carried out by first selecting the electric configuration of the element. Then various parameters are tuned, which are related to the crystal field splitting, to account for the octahedral component, the spin-orbit coupling, and the screening and mixing effects, simulated by a reduction of the Slater integrals. The intrinsic broadening of each edge, associated to lifetime effects, is simulated by convoluting the calculated natural spectra with a Lorentzian [23]. Furthermore, a Gaussian broadening of 0.2 eV is used to account for the experimental broadening and the simulation is shifted by -2.15 eV in the photon energy.

This analysis delivers the following picture: The XAS and XMCD spectra for Ni [shown in Fig. 3(a)] point towards a pure presence of octahedral Ni^{2+} (O_h) [24,25] with a crystal field splitting of $10Dq = 2.4$ eV. The calculation is performed considering the inclusion of the direct Coulomb Slater integrals F_{pd} and F_{dd} and of the exchange Coulomb integral G_{pd} , reduced to 80% to account for the interatomic mixing and screening. Moving on to Co [see Fig. 3(b)], we see a weak XMCD signal which emerges predominantly from a low presence (up to 2%) of Co^{2+} [13,26]. The low concentration of Co^{2+} marks a significant shift of Lu5BO, when compared to recently studied Tb5BO thin films, which featured a presence of up to 23% Co^{2+} [13]. The crystal field splitting used in the simulation is $10Dq = 1.75$ eV for Co^{2+} and $10Dq = 0.7$ eV for Co^{3+} . The Slater integral are reduced to 70%, 80%, and 65%, respectively, for F_{dd} , F_{pd} , and G_{pd} of Co^{2+} and to 80% of Hartree-Fock values in Co^{3+} . XAS and XMCD spectra around the $L_{2,3}$ edges of Fe indicate a dominant presence of octahedral Fe^{3+} [13,27]. A crystal field

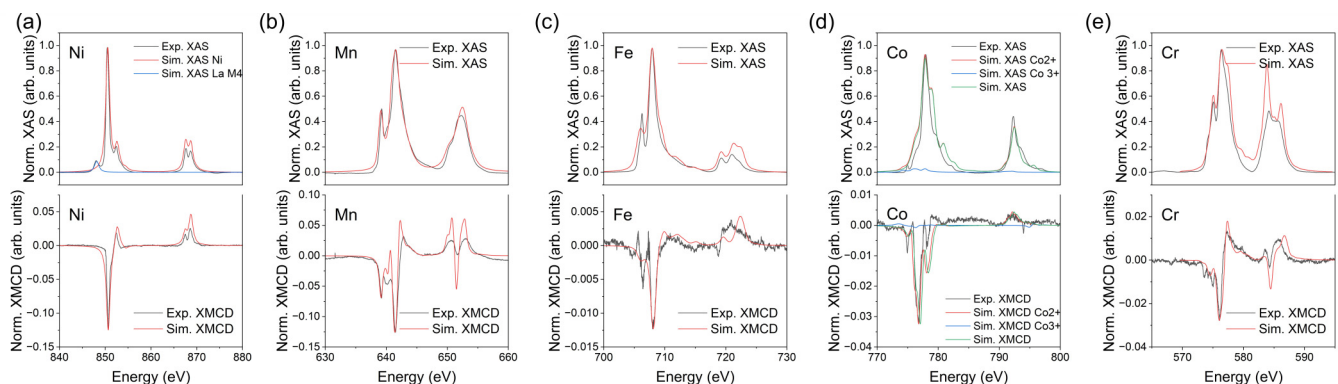


FIG. 3. X-ray absorption spectra recorded with an out-of-plane geometry (upper panel) and corresponding x-ray magnetic circular dichroism spectra (lower panel) recorded at 2.5 K. Spectra are recorded for (a) Ni, (b) Co, (c) Fe, (d) Mn, and (e) Cr.

splitting of $10Dq = 1.75$ eV is used to simulate the octahedral component of Fe^{3+} . The Slater integrals are reduced to 80% of the Hartree-Fock values. Fe appears to feature the weakest XMCD signal of all transition metal elements within Lu5BO [see Fig. 3(c)]. In Fig. 3(d) the Mn spectra reveal a dominant if not pure presence of octahedral Mn^{4+} [13,28,29]. The best match between experiment and simulation is obtained with Mn^{4+} affected by crystal field effects associated with octahedral symmetry, simulated by a crystal field splitting of $10Dq = 2.3$ eV. The Slater integral reduction amounts to 50% for F_{dd} , 40% for F_{pd} , and 50% for G_{pd} . Charge transfer effects were taken into account in the simulations, through a charge transfer energy Δ of 4.5 eV. The spectra around the Cr $L_{2,3}$ edges are consistent with a pure presence of octahedral Cr^{3+} [13,30] and are fitted with a crystal field splitting in the simulation of $10Dq = 2.0$ eV. The Slater integrals F_{dd} , F_{pd} , and G_{pd} are all reduced to 80% of their Hartree-Fock values. The charge transfer energy parameter Δ was set to 4.0 eV in the simulations.

Similar to our previous study on Tb5BO thin films, we are able to extract estimates of the orbital (m_L), spin (m_S), and total magnetic moment ($m_L + m_S$) per average transition metal ion, by applying XMCD sum rules [13,31–33] to the recorded XAS and XMCD spectra. The sum rules apply to the $2p$ and $3d$ level transition. The integrated x-ray absorption spectrum over the whole $L_{2,3}$ edge is directly proportional to the number of holes $3d n_h$. For $L_{2,3}$ XMCD spectra, the recorded signal is directly proportional to the magnetic moment of the excited transition metal ion. The orbital magnetic moment is given by

$$m_L = \frac{4}{3} n_h \frac{\int_{L_3+L_2} (\mu_{+1} - \mu_{-1})}{\int \mu},$$

where μ is the overall absorption coefficient consisting of both the absorption coefficients with individual left- and right-polarized x rays, μ_{-1} and μ_{+1} , respectively. The spin sum rule yields an integral consisting of an estimate for the spin magnetic moment m_S and contributions from spin-quadrupole coupling, which we neglect to simplify the analysis [34]. The spin sum rule is then given by

$$m_S = n_h \frac{\int_{L_3} (\mu_{+1} - \mu_{-1}) - 2 \int_{L_2} (\mu_{+1} - \mu_{-1})}{\int \mu}.$$

This way, we are able to extract the orbital (m_L) and spin (m_S) moments, in addition to the ratio (m_L/m_S). Sum rules require a good separation between the L_2 and L_3 absorption edges, which for Ni, Co, and Fe is reasonable, while early transition metal elements such as Cr and Mn require significant correction factors [35]. Leaving Cr out for these reasons, the results of these calculations are summarized in Table I. Sum-rule integrations for spectra recorded in both the grazing geometry and out-of-plane geometries for Mn, Fe, Ni, and Co and overall out-of-plane analysis can be seen in the Supplemental Material [21]). Similar to Tb5BO [13], Mn features the largest spin magnetic moment ($m_S = -1.67\mu_B$), which is more than four times larger than the next largest spin magnetic moment of Ni ($m_S = -0.35\mu_B$). Ni appears to be the element with the largest ratio of orbital and spin magnetic moments ($m_L/m_S = 0.52$), while Co occupies this spot in Tb5BO thin films [13]. To complement the sum-rule analysis

TABLE I. XMCD sum-rule analysis for four transition metal ions in Lu5BO stemming from XAS and XMCD spectra recorded in an out-of-plane geometry (6 T magnetic field employed out of plane with respect to substrate surface). Due to the large overlap of the L_2 and L_3 absorption edges in Cr and the inaccuracies that come with it, Cr was left out of the sum-rule analysis.

Element (Corr. factor)	Number of holes	m_S (μ_B)	m_L (μ_B)	m_L/m_S
Ni (0.92)	2	-0.35(2)	-0.18(4)	0.52(3)
Mn (0.59)	7	-1.67(1)	0.16(7)	-0.099(9)
Co (0.89)	3	-0.17(7)	-0.06(3)	0.35(7)
Fe (0.68)	5	-0.16(8)	0.02(5)	-0.14(8)

for the magnetic field applied out of plane, we recorded the same XAS and XMCD spectroscopy data as in Fig. 3 with a magnetic field of 6 T employed at a grazing angle of 30° with respect to the sample surface and performed a sum-rule analysis whose results are summed up in Table II. The magnetic moments derived from XAS and XMCD measurements performed in the out-of-plane and grazing incidence geometry are identical within experimental error, demonstrating the consistency of the sum-rule analysis. The only exception is the m_L value for Ni, which is small.

B. Element-sensitive magnetometry: XMCD hysteresis loops

Now, we aim to shed light into how each transition metal element contributes to the overall magnetic response in Lu5BO. This is done by recording XMCD hysteresis loops [13,36] at the L_3 edge of all involved five transition metal elements. In both out-of-plane and grazing geometry, we recorded XMCD hysteresis loops for magnetic fields between -6 and $+6$ T with a step size of 0.1 T per measurement point at temperature $T = 2.5$ K (Fig. 4). Similar to Tb5BO [13], it is Ni that exhibits the clearest hysteresis of all elements. Interestingly, the out-of-plane XMCD hysteresis loops for Ni feature what appears to be a two-step shape (see the Ni hysteresis loop in Fig. 4 upper panel), a feature observed in systems exhibiting glassy behavior [37]. The two-step magnetic response disappears for Ni, when recording XMCD hysteresis loops at the grazing angle (see the Ni hysteresis loop in Fig. 4 lower panel). The anisotropic magnetic response observed for Ni in Fig. 4 is similar to the macroscopic SQUID data in Fig. 2. In comparison to Ni,

TABLE II. XMCD sum-rule analysis for four transition metal ions in Lu5BO stemming from XAS and XMCD spectra recorded in a grazing incidence geometry (6 T magnetic field applied at an angle of 30° with respect to the sample surface).

Element (Corr. factor)	Number of holes	m_S (μ_B)	m_L (μ_B)	m_L/m_S
Ni (0.92)	2	-0.36(7)	-0.03(5)	0.09(6)
Mn (0.59)	7	-1.41(3)	0.11(5)	-0.08(1)
Co (0.89)	3	-0.09(3)	-0.02(6)	0.28(2)
Fe (0.68)	5	-0.20(2)	0.00(7)	-0.00

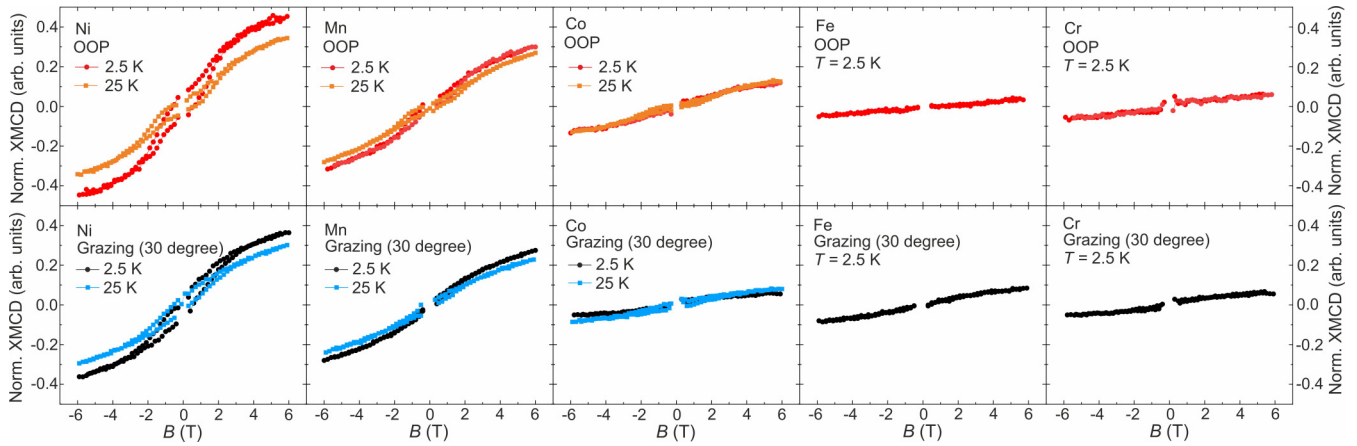


FIG. 4. XMCD hysteresis loops recorded at the L_3 edges of all involved transition metal elements at $T = 2.5$ K. XMCD hysteresis loops are recorded for magnetic fields applied out of plane (upper panel) and at a grazing angle of 30° with respect to the substrate surface (lower panel). For Ni, Mn, and Co, XMCD hysteresis loops were also recorded at 25 K (orange and blue solid squares).

Mn features a rather small opening in its hysteresis loops, both with fields applied out of plane and at a grazing angle (see Mn hysteresis loop in Fig. 4). While not shown here, these hysteresis curves disappear when heating the sample up to 50 K. The most radical difference to Tb5BO [13] is that Co, Fe, and Cr in Lu5BO show little to no hysteresis at all, down to 2.5 K (see Fig. 4). Even Mn shows quite a weak hysteresis, when compared to what was obtained for Tb5BO [13]. All together, these results correspond well to the smaller macroscopic saturation magnetization, as confirmed by SQUID magnetometry. The weaker XMCD signals for Co, Fe, and Cr may indicate that Lu5BO orders predominantly antiferromagnetically at low temperature. To confirm this, we characterize the Lu5BO thin films using element-sensitive x-ray magnetic linear dichroism (XMLD).

C. X-ray magnetic linear dichroism (XMLD)

We performed element-sensitive x-ray magnetic linear dichroism (XMLD) spectroscopy [38] at the $L_{2,3}$ absorption edges on Lu5BO thin films [see example for Fe in Figs. 5(b)–5(d)]. X-ray linear dichroism spectra usually contain several contributions including antiferromagnetism, crystal-field-induced charge anisotropy, and substrate-induced effects that are generally described as natural linear dichroism. This mixture is particularly strong at the L_3 edge making it difficult to distinguish contributions from one another. One strategy to separate magnetic contributions from other effects is to perform temperature-dependent XMLD measurements [39] and to compare the results to other measurements, for example from macroscopic magnetometry. Furthermore, contributions to linear dichroism at the L_2 edge are mostly of magnetic origins [39,40]. For this reason, we performed temperature-dependent XMLD spectroscopy focusing around the L_2 edges of the five transition metal elements [see example for Fe in Figs. 5(b) and 5(c)]. The XMLD spectra are recorded by recording XAS spectra with vertically and horizontally linear polarized x rays. Subtracting the two XAS spectra from one another delivers the desired XMLD spectra. The measurements are performed at zero magnetic field and a grazing angle of 30° with respect to the sample surface.

Plotting the intensity of the L_2 XMLD signal at the C and D peaks of the XAS spectra [see Fig. 5(b) and red and black arrows in Fig. 5(c)] as a function of temperature, we see an interesting picture emerging: The clearest temperature-dependent trends of the XMLD signal as a function of temperature are observed for Fe and Mn, with their XMLD signals vanishing close to 100 K [see Fig. 5(d) and 5(e)]. The temperature-dependent XMLD signal for Co appears to remain constant throughout the explored temperature range [see Fig. 5(f)], indicating that this can be largely attributed to so-called natural or substrate-induced dichroism. The XLD signal for Ni decays with temperature [see Fig. 5(g)], but more slowly than the corresponding signals for Fe and Mn. Finally, Cr exhibits a temperature-dependent XMLD that resembles the trends observed for Mn and Fe [see Fig. 5(h)]. Recording XMLD spectra with a magnetic field of 2 T applied in two directions (see Supplemental Table 1 [21]), first along the z direction (parallel to the incoming x rays), then along the x direction [see schematic in Fig. 5(a)] yield no change in the dichroism signals for Fe, Cr, and Mn, with minor changes observed at the L_3 edges of Ni and Co. Overall, it confirms that the temperature-dependent trends in the XMLD signals for Fe, Cr, and Mn correspond to their antiferromagnetism resulting in dominant antiferromagnetic order in Lu5BO thin films grown on STO (001) substrates.

IV. SUMMARY, CONCLUSIONS, AND OUTLOOK

In summary, we have performed a full-scale element-sensitive x-ray absorption spectroscopy and magnetometry study on Lu5BO thin films grown on STO (001), adding a member to the HEOP thin film family. Element-sensitive XMCD and XMLD spectroscopy strongly hint towards Lu5BO exhibiting an antiferromagnetic phase below 100 K. A comparison to recently studied Tb5BO [13] reveals that Lu5BO exhibits a radically reduced Co^{2+} concentration of up to only 2%, which can be seen as a main driver for the smaller net magnetic moment. This drastic reduction in the presence of Co^{2+} is likely driven by the lack of tensile strain and the relaxed nature of Lu5BO thin films grown on STO (001)

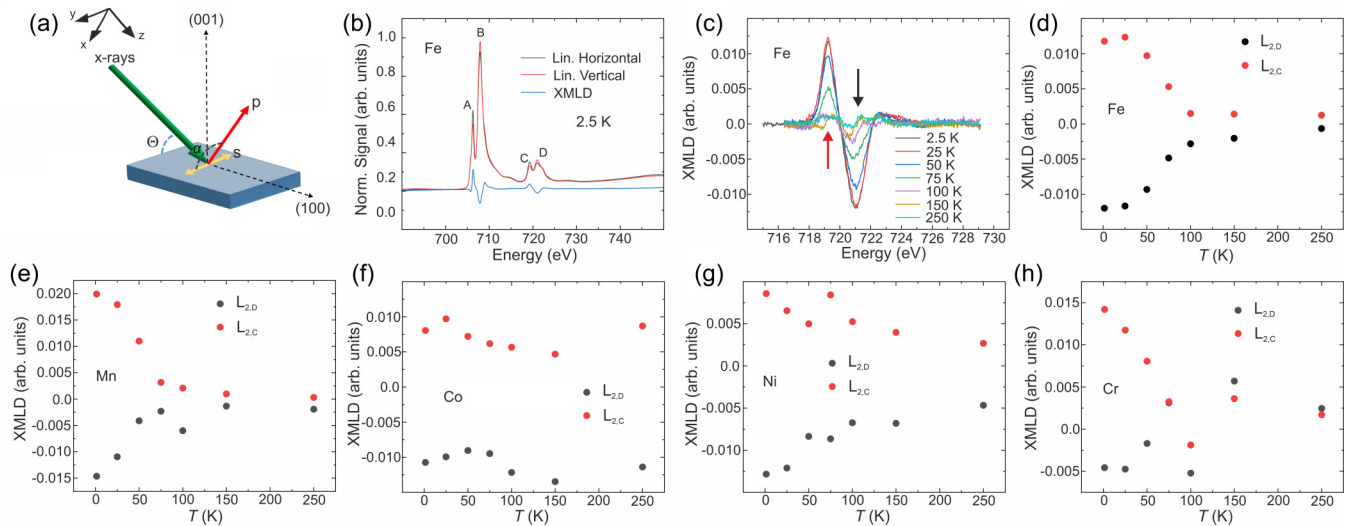


FIG. 5. (a) Sketch of the XMLD measurement geometry, with spectra recorded with vertical ($\alpha = 90^\circ$) and horizontal ($\alpha = 0^\circ$) polarized x-rays. The angle of incidence Θ is set at 30° . (b) Normalized XAS recorded with vertically (red curve) and horizontal (black) linear polarized light and XMLD spectrum (blue curve) recorded at 2.5 K around the Fe $L_{2,3}$ edges. (c) XMLD spectra at the Fe L_2 recorded at various temperatures between 2.5 and 250 K. The red and black arrows indicate the XMLD maxima C and D, respectively, which are then plotted as a function of temperature for (d) Fe, (e) Mn, (f) Co, (g) Ni, and (h) Cr. The data are recorded at zero-field conditions. Complementary XMLD measurements at 2.5 K and a magnetic field of 2 T applied along the z and x directions are summarized in Supplemental Table 1 and Supplemental Table 2 [21].

substrates, similar to observations on the $\text{Co}^{2+}/\text{Co}^{3+}$ ratio in LaCoO_3 thin films grown on various substrates [41]. This notion opens up a viable route for tuning the presence of Co^{2+} in HEOP thin films via epitaxial strain. Other effects worth exploring include a variation of the stoichiometry within the transition metal 5B block [11] or the mixing of Tb and Lu with other rare-earth ions at the rare-earth ion sites. Our findings on the stabilization and element-sensitive characterization of the magnetic order in Tb- and Lu-based orthorhombic HEOP thin films provide a stepping stone towards the potential stabilization of hexagonal h-Lu5BO or h-Tb5BO, when grown on selected substrates, in analogy to multiferroic parent compounds such as h-LuFeO₃ [14] or h-TbMnO₃ [42], and the potential emergence of the first multiferroic HEOP thin films.

ACKNOWLEDGMENTS

The authors thank A. Kleibert and Y.-L. Huang for their support and fruitful discussions. This work was supported by the Academy of Finland (Project No. 316857) and part of this work was performed at the XTreme beamline of the Swiss Light Source. F.S. is funded by the Swiss National Science Foundation (SNF) (Grant No. 200021_184684). SQUID-VSM measurements were carried out on the Quantum Design MPMS3-137 device of the Laboratory for Mesoscopic Systems, ETH Zurich, Switzerland and the Laboratory for Multiscale Materials Experiments, Paul Scherrer Institute, Switzerland. We acknowledge the provision of facilities and technical support by Aalto University at OtaNano - Nanomicroscopy Center (Aalto-NMC).

- [1] C. M. Rost, E. Sachet, T. Borman, A. Moballeggh, E. C. Dickey, D. Hou, J. L. Jones, S. Curtarolo, and J.-P. Maria, *Nat. Commun.* **6**, 8485 (2015).
- [2] R.-Z. Zhang and M. J. Reece, *J. Mater. Chem. A* **7**, 22148 (2019).
- [3] E. P. George, D. Raabe, and R. O. Ritchie, *Nat. Rev. Mater.* **4**, 515 (2019).
- [4] D. Bérardan, S. Franger, D. Dragoe, A. Kumar Meena, and N. Dragoe, *Phys. Status Solidi RRL* **10**, 328 (2016).
- [5] P. A. Krawczyk, M. Jurczyszyn, J. Pawlak, W. Salamon, P. Baran, A. Kmita, L. Gondek, M. Sikora, C. Kapusta, T. Straczek, J. Wyrwa, and A. Żywczak, *ACS Appl. Electron. Mater.* **2**, 3211 (2020).
- [6] J. L. Braun, C. M. Rost, M. Lim, A. Giri, D. H. Olson, G. N. Kotsonis, G. Stan, D. W. Brenner, J.-P. Maria, and P. E. Hopkins, *Adv. Mater.* **30**, 1805004 (2018).
- [7] R. Witte, A. Sarkar, R. Kruk, B. Eggert, R. A. Brand, H. Wende, and H. Hahn, *Phys. Rev. Mater.* **3**, 034406 (2019).
- [8] R. Witte, A. Sarkar, L. Velasco, R. Kruk, R. A. Brand, B. Eggert, K. Ollefs, E. Weschke, H. Wende, and H. Hahn, *J. Appl. Phys.* **127**, 185109 (2020).
- [9] Y. Sharma, Q. Zheng, A. R. Mazza, E. Skoropata, T. Heitmann, Z. Gai, B. Musico, P. F. Miceli, B. C. Sales, V. Keppens, M. Brahlek, and T. Z. Ward, *Phys. Rev. Mater.* **4**, 014404 (2020).
- [10] Y. Sharma, B. L. Musico, X. Gao, C. Hua, A. F. May, A. Herklotz, A. Rastogi, D. Mandrus, J. Yan, H. N. Lee, M. F. Chisholm, V. Keppens, and T. Z. Ward, *Phys. Rev. Mater.* **2**, 060404(R) (2018).
- [11] A. R. Mazza, E. Skoropata, Y. Sharma, J. Lapano, T. W. Heitmann, B. L. Musico, V. Keppens, Z. Gai, J. W. Freeland, T. R. Charlton, M. Brahlek, A. Moreo, E. Dagotto, and T. Z. Ward, *Adv. Sci.* **9**, 2200391 (2022).

- [12] A. R. Mazza, E. Skoropata, J. Lapano, J. Zhang, Y. Sharma, B. L. Musico, V. Keppens, Z. Gai, M. J. Brahlek, A. Moreo, D. A. Gilbert, E. Dagotto, and T. Z. Ward, *Phys. Rev. B* **104**, 094204 (2021).
- [13] A. Farhan, F. Stramaglia, M. Coconcelli, N. Kuznetsov, L. Yao, A. Kleibert, C. Piamonteze, and S. van Dijken, *Phys. Rev. B* **106**, L060404 (2022).
- [14] J. A. Moyer, R. Misra, J. A. Mundy, C. M. Brooks, J. T. Heron, D. A. Muller, D. G. Schlom, and P. Schiffer, *APL Mater.* **2**, 012106 (2014).
- [15] J. A. Mundy, C. M. Brooks, M. E. Holtz, J. A. Moyer, H. Das, A. F. Rébola, J. T. Heron, J. D. Clarkson, S. M. Disseler, Z. Liu, A. Farhan, R. Held, R. Hovden, E. Padgett, Q. Mao, H. Paik, R. Misra, L. F. Kourkoutis, E. Arenholz, A. Scholl, J. A. Borchers *et al.*, *Nature (London)* **537**, 523 (2016).
- [16] A. M. Zhang, H. F. Cao, X. X. Pan, J. J. Zhu, and X. S. Wu, *Thin Solid Films* **750**, 139186 (2022).
- [17] J. A. Alonso, M. J. Martínez-Lope, M. T. Casais, J. L. García-Munoz, and M. T. Fernández-Díaz, *Phys. Rev. B* **61**, 1756 (2000).
- [18] C. Piamonteze, U. Flechsig, S. Rusponi, J. Dreiser, J. Heidler, M. Schmidt, R. Wetter, M. Calvi, T. Schmidt, H. Pruchova, J. Krempasky, C. Quitmann, H. Brune, and F. Nolting, *J. Synchrotron Radiat.* **19**, 661 (2012).
- [19] Y. Wu, J. Stohr, B. D. Hermsmeier, M. G. Samant, and D. Weller, *Phys. Rev. Lett.* **69**, 2307 (1992).
- [20] Y.-L. Huang, D. Nikonov, C. Addiego, R. V. Chopdekar, B. Prasad, L. Zhang, J. Chatterjee, H.-J. Liu, A. Farhan, Y.-H. Chu, M. Yang, M. Ramesh, Z. Q. Qiu, B. D. Huey, C.-C. Lin, T. Gosavi, J. Íñiguez, J. Bokor, X. Pan, I. Young, L. W. Martin *et al.*, *Nat. Commun.* **11**, 2836 (2020).
- [21] See Supplemental Material at <http://link.aps.org/supplemental/10.1103/PhysRevMaterials.7.044402> for details of the sum rule analysis and summarizing tables for the in-field XMLD measurements.
- [22] E. Stavitski and F. M. F. de Groot, *Micron* **41**, 687 (2010).
- [23] M. O. Krause and J. H. Oliver, *J. Phys. Chem. Ref. Data* **8**, 329 (1979).
- [24] J. Lumetzberger, M. Buchner, S. Pile, V. Ney, W. Gaderbauer, N. Daffé, M. V. Moro, D. Primetzhofner, K. Lenz, and A. Ney, *Phys. Rev. B* **102**, 054402 (2020).
- [25] C. Klewe, M. Meinert, A. Boehnke, K. Kuepper, E. Arenholz, A. Gupta, J.-M. Schmalhorst, T. Kuschel, and G. Reiss, *J. Appl. Phys.* **115**, 123903 (2014).
- [26] C. Moya, A. Fraile Rodríguez, M. Escoda-Torroella, M. García del Muro, S. R. V. Avula, C. Piamonteze, X. Batlle, and A. Labarta, *J. Phys. Chem. C* **125**, 691 (2021).
- [27] R. V. Chopdekar, M. Liberati, Y. Takamura, L. F. Kourkoutis, J. S. Bettinger, B. B. Nelson-Cheeseman, E. Arenholz, A. Doran, A. Scholl, D. A. Muller, and Y. Suzuki, *J. Magn. Magn. Mater.* **322**, 2915 (2010).
- [28] J.-S. Kang, S. M. Lee, D. H. Kim, S. Kolesnik, B. Dabrowski, B.-G. Park, J.-Y. Kim, J. Lee, B. Kim, and B. I. Min, *J. Appl. Phys.* **107**, 09D721 (2010).
- [29] C. Mitra, Z. Hu, P. Raychaudhuri, S. Wirth, S. I. Csiszar, H. H. Hsieh, H.-J. Lin, C. T. Chen, and L. H. Tjeng, *Phys. Rev. B* **67**, 092404 (2003).
- [30] G. Vinai, A. Khare, D. S. Rana, E. Di Gennaro, B. Gobaut, R. Moroni, A. Yu. Petrov, U. Scotti di Uccio, G. Rossi, F. Miletto Granozio, G. Panaccione, and P. Torelli, *APL Mater.* **3**, 116107 (2015).
- [31] B. T. Thole, P. Carra, F. Sette, and G. van der Laan, *Phys. Rev. Lett.* **68**, 1943 (1992).
- [32] P. Carra, B. T. Thole, M. Altarelli, and X. Wang, *Phys. Rev. Lett.* **70**, 694 (1993).
- [33] C. T. Chen, Y. U. Idzerda, H.-J. Lin, N. V. Smith, G. Meigs, E. Chaban, G. H. Ho, E. Pellegrin, and F. Sette, *Phys. Rev. Lett.* **75**, 152 (1995).
- [34] C. Piamonteze, P. Miedema, and F. M. F. de Groot, *Phys. Rev. B* **80**, 184410 (2009).
- [35] Y. Teramura, A. Tanaka, and T. Jo, *J. Phys. Soc. Jpn.* **65**, 1053 (1996).
- [36] B. B. Nelson-Cheeseman, R. V. Chopdekar, J. S. Bettinger, E. Arenholz, and Y. Suzuki, *J. Appl. Phys.* **103**, 07B524 (2008).
- [37] B. Pang, L. Zhang, Y. B. Chen, J. Zhou, S. Yao, S. Zhang, and Y. Chen, *ACS Appl. Mater. Interfaces* **9**, 3201 (2017).
- [38] J. Lüning, F. Nolting, A. Scholl, H. Ohldag, J. W. Seo, J. Fompeyrine, J.-P. Locquet, and J. Stöhr, *Phys. Rev. B* **67**, 214433 (2003).
- [39] T. Zhao, A. Scholl, F. Zavaliche, K. Lee, M. Barry, A. Doran, M. P. Cruz, Y. H. Chu, C. Ederer, N. A. Spaldin, R. R. Das, D. M. Kim, S. H. Baek, C. B. Eom, and R. Ramesh, *Nat. Mater.* **5**, 823 (2006).
- [40] K.-T. Ko, M. H. Jung, Q. He, J. H. Lee, C. S. Woo, K. Chu, J. Seidel, B.-G. Jeon, Y. S. Oh, K. H. Kim, W.-I. Liang, H.-J. Chen, Y.-H. Chu, Y. H. Jeong, R. Ramesh, J.-H. Park, and C.-H. Yang, *Nat. Commun.* **2**, 567 (2011).
- [41] G. Zhou, X. Wang, H. Ji, J. Zhang, P. Kang, Z. Li, and X. Xu, *J. Magn. Magn. Mater.* **515**, 167303 (2020).
- [42] D. J. Kim, T. R. Paudel, H. Lu, J. D. Burton, J. G. Connell, E. Y. Tsymbal, S. S. A. Seo, and A. Gruverman, *Adv. Mater.* **26**, 7660 (2014).